Available online at www.sciencedirect.com
ScienceDirect
International Journal of Heat and Mass Transfer 50 (2007) 3809–3819
International Journal of HEAT and MASS TRANSFER
www.elsevier.com/locate/ijhmt

Microstructures and macroscopic conductivity of randomly packed and uniaxially pressed sphere compacts

Isao Taguchi [a,*], Michio Kurashige [b]

[a] Graduate School of Engineering, Iwate University, Ueda 4-3-5, Morioka, Iwate 020-8551, Japan
[b] Department of Mechanical Engineering, Iwate University, Ueda 4-3-5, Morioka, Iwate 020-8551, Japan

Received 9 August 2006; received in revised form 19 January 2007
Available online 16 April 2007

Abstract

The present paper deals with simulation of microstructures and macroscopic conductivity of randomly packed, uniaxially pressed and sintered particles. Random packings of identical spheres are constructed by using a sequential deposition method and their microgeometry after the compaction in sintering is geometrically created by proportional reduction in distances between the sphere centers only in the vertical direction and by mass addition around overlapped necks. Some of microgeometrical characteristics of the created compacts are statistically examined. Using the data on the packings and geometrical models, macroscopic thermal conductivities of the compacts are estimated. It is found that the conductivities are greatly different from those of simple cubic packings, although both the packings have almost the same coordination number, and that anisotropy in the conductivity is induced by the compaction in addition to gravity. The conductivities are expressed as a function of the compaction and sintering degrees for practical purposes.

Keywords: Thermal conductivity; Random packing; Microstructure; Uniaxial pressing; Sintering; Transverse isotropy

1. Introduction

Porous materials have enhanced material properties in thermal insulation, specific moduli, specific strength and wear resistance in comparison with pure materials [1]. Various methods of manufacturing such functional porous materials are available, such as foaming and powder sintering. Powder sintering is one of the most common and easiest methods. We will deal with the porous materials prepared by powder sintering or sintering of randomly packed microspheres.

It is important to evaluate various thermal and mechanical properties of the sintered aggregate of powder for their practical applications and their material design. Hence, development of some good evaluation method is needed.

As a strong tool to evaluate various material properties, we have some composite material models such as the self-consistent model [2]. These models have been applied to evaluation of the properties of spherical particle aggregates [2,3]. However, any of the models can describe neither their complicated pore geometry nor the geometry of necks connecting spheres, probably resulting in poor estimation.

To avoid this difficulty, Kurashige et al. [4] proposed a simulation method to calculate the elastic properties of a random packing of identical spheres by replacing the real arrangement by a random network of springs of six degrees of freedom. The results by this simulation were in good agreement with experimental ones.

It is well known that the macroscopic properties of sintered powder strongly depend on microscopic characteristics such as porosity and the ways of packing. Kurashige et al. [5] and Kato et al. [6] extracted some statistical characteristics of random packing structures from the data on the random packings; no statistical information of the packings can be provided by other models such as the self-consistent

* Corresponding author. Address: Aomori Prefectural Agriculture and Forestry Research Center, Inuotose-Yanagisawa 91, Rokunohe, Aomori 033-0071, Japan. Tel.: +81 176 53 7171; fax: +81 176 53 8934.
E-mail address: isao_taguchi@pref.aomori.lg.jp (I. Taguchi).

0017-9310/$ - see front matter © 2007 Elsevier Ltd. All rights reserved.
doi:10.1016/j.ijheatmasstransfer.2007.02.007

Nomenclature

B	box size, i.e., side length of virtual cubic box
c	viscosity constant
D	diameter of spherical particle
$\boldsymbol{d}$	overlapping depth vector between two spheres in collision
g	gravitational acceleration
$g_2(r)$	radial distribution function
h	overlapping depth of particle pair
$H()$	Heaviside step function
$\boldsymbol{k}$	unit base vector along z-axis
k	spring constant between particles in collision
K	inverse of axial thermal resistance of compacted sintered pair of spheres
K_0	inverse of axial thermal resistance of cylindrical solid bar with same diameter and length of spherical particles
m	mass of each particle
Q_{total}	total heat flow rate
R	radius of spherical particle
R_i	resistance of ith resistor
r_0	meniscus radius representing sintering degree
r, θ, φ	spherical polar coordinate
r_{neck}	neck radius
T	temperature
t	time
V_{add}	added-mass volume per pair of particles
V_{lap}	overlapping volume per pair of particles
$\boldsymbol{x}$	position vector of falling sphere's center
z_i	z-coordinate of ith sphere center before compaction
Z_i	z-coordinate of ith sphere center after compaction

Greek symbols

β	compaction degree coefficient
ε	small parameter to define settlement of each particle
κ	macroscopic thermal conductivity
κ_0	thermal conductivity of particle substance
ϕ	volume (or bulk) porosity
Φ	volume (or bulk) porosity of sintered aggregate
ρ_0	number density
Θ	sintering degree angle

model. In addition, they estimated thermal and mechanical properties by the same evaluation method as that in [4] and discussed relations of them to the statistical characteristics. The thermal conductivity and elastic moduli of the sintered aggregates are of transverse isotropy, which is caused by the deviated microstructures of the packings.

In the process of fabrication, uniaxial or isostatic compaction of particles is a typical industrial route to obtain metal compacts with low porosity [7,8]. In general, powder compacts are obtained via cold or hot uniaxial compaction or hydrostatic pressing in a first step. A secondary step may involve pressureless sintering or severe plastic deformation at high temperature, depending on final applications [9–13]. The above simulations [4–6] do not take into account effects of the compaction on the macroscopic mechanical properties.

This paper deals with microstructures and macroscopic conductivity of randomly packed, uniaxially compacted/sintered particles. We focus on an effect of the uniaxial compaction in the fabrication process on the microstructures and macroscopic conductivity. We use the same simulation method as that for the identical sphere aggregates by Kurashige et al. [5]. This method is appropriate to evaluate various properties of the sintered particle aggregates in the sense that it can correctly describe the geometries of space among particles and of necks.

We construct the packings of particles using a method of sequential deposition of particles and examine statistical properties such as radial distribution functions, coordination numbers and directional distribution of line segments connecting centers of particles in contact. Then, we evaluate the thermal conductivity of the uniaxially compacted sintered spherical particle aggregates and discuss its behavior in terms of the degrees of compaction and sintering with its relations to the statistical properties.

2. Construction of microgeometrical model

2.1. Random packing and equation of motion

To generate a spherical particle random packing in a computer, we carry out a simulation of particle's free fall into a virtual box. We sequentially throw identical spherical particles with diameter D from random positions into the box. For the simplification of calculation, we assume that a falling particle is subjected to only gravity and forces from resting particles when collided with them, leading to negligence of the inertia force on it, its friction against other particles in contact, its rotation and adhesion to others. Thus, the motion equation of the particle can be expressed as follows:

$$c\frac{\mathrm{d}\boldsymbol{x}}{\mathrm{d}t} = \sum k\Delta\boldsymbol{d} - mg\boldsymbol{k}, \tag{1}$$

where $\boldsymbol{x}$ is the position vector of a falling sphere's center, $\boldsymbol{k}$ is the unit vector along the z axis and $\Delta\boldsymbol{d}$ is the overlapping depth vector of the particle in collision with another still one. Summation notation $\sum$ is over the number of all

particles in contact with the one under consideration. Notations c, k, m and g are the viscosity constant, the spring constant between two or more particles in collision, the mass of each sphere and the gravitational acceleration, respectively.

The center coordinates $\boldsymbol{x}$ of the particle at a time t can be obtained by solving the motion equation. We use the Runge–Kutta–Gill method to solve the three coupled differential equations; in other words, we calculate coordinates of the particle's center at each discrete time with time increment Δt. If the distance over which the particle moves during Δt is smaller than some given small value ε, we judge that it has stopped and then throw a new particle into the box. Repetition of this throw-in until the box is fully filled with particles constructs a complete packing.

In running our program, we use the following non-dimensional numerical values, taking spherical particle diameter D as a reference length: time increment $\Delta T = \Delta t/(mg/cD) = 1.0 \times 10^{-3}$, spring constant $K = Dk/(mg) = 1.0 \times 10^{3}$ and small parameter $\varepsilon = 1.0 \times 10^{-7}$, employed in Taguchi et al. [14].

2.2. Simulation method

Consider a virtual box of $0 \leqslant x \leqslant B$, $0 \leqslant y \leqslant B$, $0 \leqslant z \leqslant H(B < H)$. We do not stop introducing particles until the region $0 \leqslant x \leqslant B$, $0 \leqslant y \leqslant B$, $0 \leqslant z \leqslant 1.5B$ is completely filled with particles. We continue the particle introduction up to $z = 1.5B$ because we need the margin for compaction. We adopt box sizes $B/D = 16$ and five runs are made with five different sets of pseudorandom numbers.

Effects of boundaries of the virtual box in which spheres accumulate are eliminated by introducing the periodic boundary conditions on its walls. The level of the box floor is displaced up and down within the range of D for each sphere by the magnitude given by pseudorandom numbers in order to avoid packing regularity on the floor. These random numbers are generated by the algorithm of Wichmann and Hill [15].

2.3. Modeling of compaction and sintering

Several mechanisms can be involved in powder compaction processes [9–13]: rearrangement and densification of particles, corruption of large voids, and plastic deformation of particles. All these mechanisms are connected with each other and affected by friction between particles, adhesion of particles and so on. It is difficult to predict them and their connection as well as various affecting factors. Therefore, we will not simulate all this process. Furthermore, we need not know the whole densification process; we need only the resulting microgeometry of the compacted/sintered aggregate. To describe the compacted geometry, we introduce a new scaled coordinate of each sphere center as follows:

$$Z_i = (1 - \beta) z_i \tag{2}$$

where z_i and Z_i are the z-coordinates of ith sphere center before and after compaction, respectively, and β is the coefficient describing degree of the compaction, varying from 0 to 0.2 with 0.01 increment; $\beta = 0$ means no compaction. It must be noted that each sphere remains spherical in spite of the center coordinate scaling.

It should be clearly said that negligence of the particle rearrangement in the present context leads to an approximate result as compared to more sophisticated methods and to less anisotropic microstructures, as pointed out by Martin et al. [11] and others.

The compaction modeled in this way leaves overlapping of spheres, so that each neck resulting from the overlapping has a different diameter, depending on the neck orientation. To model the sintering, we add some mass around all necks so as to give the identical meniscus radius to all the necks. Here again, we do not simulate the whole sintering process but assume the neck geometry which is expected to result from the sintering. In what follows, we will use two models of the compaction and sintering: a model in which the compaction degree β and the meniscus radius r_0 (see Fig. 5 in Section 4) are independently selected (two-parameter model), and another model where the overlapping volume is transported to around the neck so as to conserve the mass by equating the overlapping volume to the neck volume (conservation model).

Here, the following should be noted: Although the volume reduction by the compaction and the volume addition by the sintering in the former model seem to violate the mass conservation, this is not the case because the macroscopic thermal conductivity depends only on shape or geometry but not on dimension; that is, the similarity law holds for the conductivity. The geometry of the compacted and sintered spheres can be adjusted to the real one by adjusting the two independent parameters of compaction and sintering degrees. Furthermore, the two-parameter model is necessary to describe microgeometry of the compacts made by soldering or brazing.

Finally, we extract a cubic region $B \times B \times B$ from a scaled region of the original $0 \leqslant X \leqslant B$, $0 \leqslant Y \leqslant B$, $0 \leqslant Z \leqslant 1.5B$. We obtain 105 samples in total (five samples times 21 scales), for each of which a list of the center coordinates of all resting particles is prepared. These lists will be used to obtain the statistical characteristics of each sample and the macroscopic conductivity of compacted/sintered particles later on.

Fig. 1 shows three dimensional random packing structures. Fig. 1a and b shows the cases of no compaction ($\beta = 0.0$) and considerable compaction ($\beta = 0.2$) for Sample 1, respectively. Scrutinizing the figure, we can see the displaced spheres in Fig. 1b corresponding to the original ones in Fig. 1a, for example as shown by the circles, and many new spheres coming into the box from the upper margin in Fig. 1b. The left aggregate is composed of 4597 spheres, while the right one contains 5702 spheres.

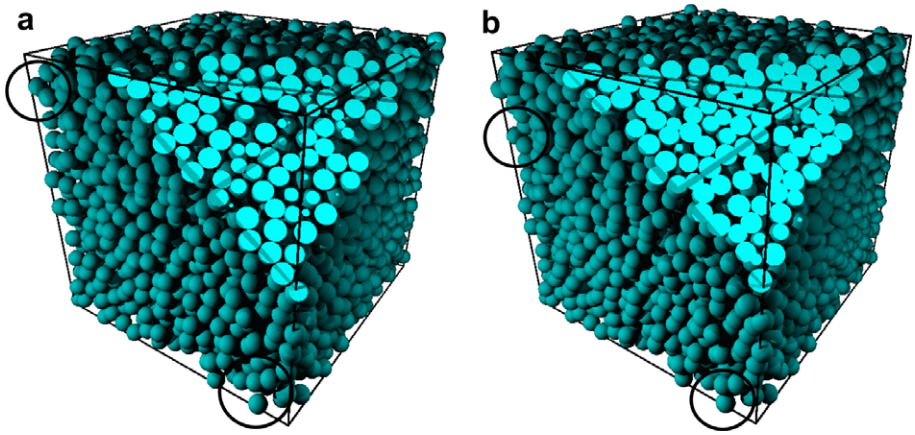

Fig. 1. Three-dimensional random packing structures: (a) before compaction ($\beta = 0.0$) and (b) after compaction ($\beta = 0.2$).

3. Microstructures of uniaxially compacted aggregates

3.1. Porosity

The averaged porosity of the random packings constructed by the above method before the compaction is approximately 41.7%. It is shown that the present packings fall in the category of random loose packing [16,17]. In addition, since this value is very close to the value (41%) obtained for the most slightly sintered glass-bead aggregates by experiments [18], the present packing method is justified even though various simplifying assumptions have been made, including negligence of the acceleration term in the motion equation.

Fig. 2 shows the change in porosity due to the uniaxial compaction in the z direction for the two compaction/sintering models. The porosity after compaction for the mass-conservation model is presented by a solid line with no marker; this is given by $\Phi = (\phi - \beta)/(1 - \beta)$ with ϕ being the porosity before compaction. The porosities for the two-parameter model are also drawn for meniscus radii $r_0/R = 0.0$, 0.12 and 0.2. Note that at $\beta = 0$ the porosity by the conservation model coincides with that by the two-parameter model with $r_0/R = 0.0$, that is, $\Phi = \phi = 0.417$ and that the curves by the two models bifurcate as β increases; the porosity by the conservation model decreases more. It is also seen that the curve of porosity by the two-parameter model falls as a whole as the meniscus radius increases. It should be noted that the porosity does not simply depend on the meniscus radius and the compaction degree, because the added volume even for the constant radius also depends on distribution of the orientations of necks against their compaction direction. This dependence proves that the distribution of neck orientations has a statistical (not analytical) effect on the porosity and subsequently that the simulation of random packing is, even by any method, indispensable to evaluate the porosity when any model rather than the conservation model is adopted.

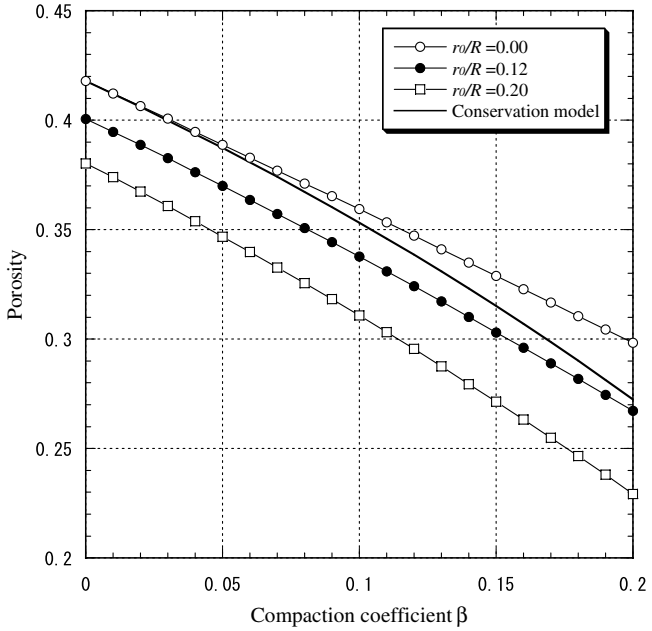

Fig. 2. Porosity verses compaction coefficient.

3.2. Radial distribution function

For particle systems, one of the most basic descriptors is a radial distribution function. The radial distribution function is defined by [19]

$$g_2(r) = \frac{1}{\rho_0}\frac{n(r)}{4\pi r^2 \Delta r}, \tag{3}$$

where ρ_0 is the number density and $n(r)$ is the number of particles contained in a concentric shell of finite thickness Δr at radial distance r from a reference particle. The radial distance r is assumed to be midway between the inner radius $r - \Delta r/2$ and outer radius $r + \Delta r/2$ of the shell.

In calculating the radial distribution function for the random packings obtained above, we adopt a particle, as a reference, which exists within the central cubic region $6D \times 6D \times 6D$. We give $\Delta r = 0.01$.

Fig. 3 shows the radial distribution function versus non-dimensional radius r/D for compaction coefficient $\beta = 0$,

0.1 and 0.2. For $\beta = 0$, we can see that the radial distribution function is zero from $r/D = 0.0$ to $r/D = 1.0$; it discontinuously jumps up to the first sharp peak at exactly $r/D = 1.0$, which corresponds to the non-overlapping (no compaction) condition. Then, the distribution function falls discontinuously and further decreases down to the minimum value at approximately $r/D = 1.5$. It has a second peak at $r/D = 2.0$ due to next-nearest neighbors. This peak has a cliff on its right side, as may be characteristic of the random loose packings. In contrast, such a peak does not appear for the case of sparsely distributed hard spheres [20], because fewer spheres are in contact with each other.

Let us examine the cases of $\beta = 0.1$ and 0.2. The first peak appears at $r/D = 1.0$ for the both cases as well, but the slope starts to rise up at $r/D = 0.8$ and 0.9 and climbs toward the peak because the distance between sphere centers in the compaction direction is shorter. For the distance larger than $r/D = 1.0$, the curves for these cases are similar to that for the case of $\beta = 0.1$. However, the second peak moves toward the smaller distance correspondingly to the compaction degree and there is no cliff behind this peak, as is also due to the uniaxial compaction.

We have been saying that the present packings are random ones, but the radial distribution function for $\beta = 0$, which has the two discontinuities, asserts that the contact of hard spheres in the packings cannot avoid to introduce some regularity in some sense; the distance between spheres in contact equals their diameter.

3.3. Coordination number

We examine coordination numbers for the random packings constructed by the above method. The coordination number is defined as the number of contact points of a particle with neighboring ones in a regular or irregular packing of particles. For a particle aggregate, electric current or heat is conducted through those contact points. Therefore, it is important to estimate the coordination number to know conductivities of the particle aggregate. With a few regular packings, it is six for a simple cubic and 12 for a compact hexagonal packing; in contrast, there is a possibility that a sphere is in contact with 4–12 other spheres for the random packing.

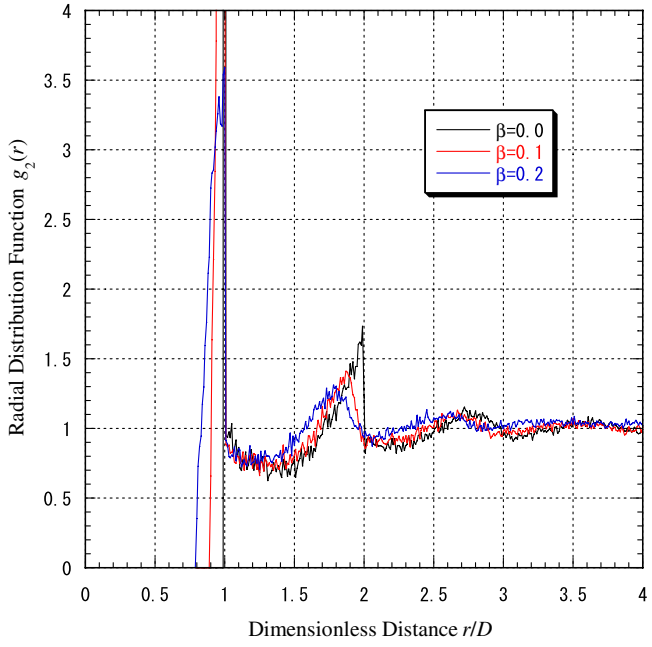

Fig. 3. Radial distribution function versus dimensionless distance for compaction coefficient $\beta = 0.0$, 0.1 and 0.2.

Table 1 shows the averaged value of the mean coordination numbers for all particles over all the samples and standard deviation for the five samples. In the case of no compaction, the average value of 6.019 is almost the same as that obtained in Taguchi and Kurashige [20], as we have used the same procedures as theirs. The average coordination number increases with increasing compaction coefficient, because the compaction creates new contact points.

Fig. 4 shows the distribution of coordination numbers averaged over all samples for the compaction coefficients $\beta = 0$, 0.1 and 0.2. For $\beta = 0$, the coordination distribution has its peak at 6 and ranges from 4 to 8. We have negligibly small and exceptional coordination numbers of 3 and 9; no sphere has more than 10 contact points. On the other hand, for $\beta = 0.2$, the coordination distribution has its peak at 7 and ranges from 4 to 10. This is also because the compaction creates new contact points.

3.4. Distribution of branch orientations

A "branch" is defined as a segment connecting the centers of spheres in contact; the spheres are judged to be in contact if the length of branch is equal to or smaller than the diameter of sphere D and not in contact if larger.

Taguchi and Kurashige [20] examined cumulative distributions of the branch orientations in the similar but non-compacted random packings. They concluded that the peak in the zenithal distributions appears around 50.1° from the vertical line, while the distributions are uniform in the horizontal plane. In the present paper, we examine how the distributions are affected by the uniaxial compaction.

Table 1
Mean coordination numbers and its standard deviation

Compaction coefficient β	Mean coordination numbers	Standard deviation
0.00	6.018858	0.002709
0.02	6.091541	0.007103
0.04	6.167563	0.010427
0.06	6.241195	0.012220
0.08	6.326158	0.013814
0.10	6.408745	0.013436
0.12	6.493894	0.014931
0.14	6.581810	0.015447
0.16	6.676293	0.016648
0.18	6.776617	0.017399
0.20	6.876486	0.018893

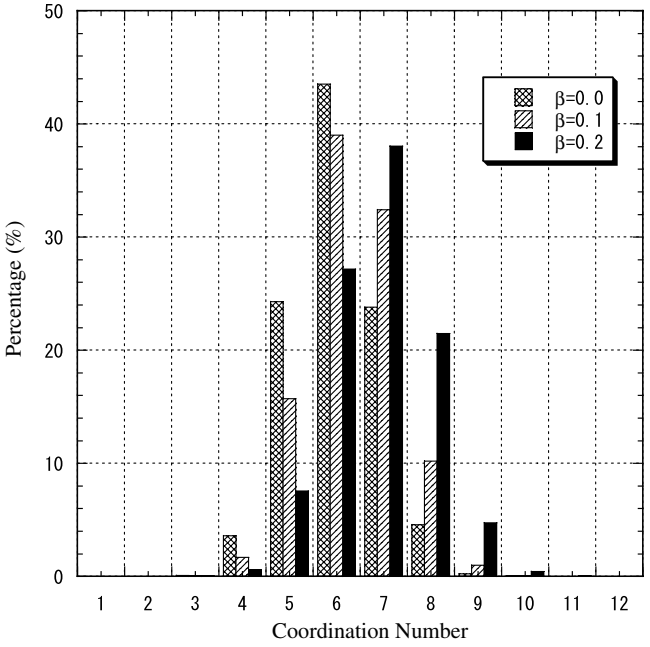

Fig. 4. Coordination number distribution for compaction coefficient $\beta = 0.0$, 0.1 and 0.2.

Before calculating both the angular distributions, let us introduce the spherical polar coordinate (r, θ, φ), where θ and φ are the zenithal and azimuthal angles, respectively; the zenithal angle is measured from the z-(vertical) axis, while the azimuthal angle is from the x-axis in the x–y plane. The zenithal and azimuthal angles of the kth branch ($k = 1, 2, \ldots, N$, with N being the total number of branches) are denoted by θ_k and φ_k, respectively.

First, to examine the azimuthal distribution of branch orientations, consider the domain of φ, $(-\pi/2, \pi/2]$. If φ_k is in $(\pi/2, \pi]$, φ_k should be replaced by $\varphi_k - \pi$; similarly, that in $(-\pi, \pi/2]$ by $\varphi_k + \pi$. Furthermore, we rearrange the branches in ascending order of azimuthal angles in the range of $(-\pi/2, \pi/2]$. We define the cumulative frequency of the branch orientations in the following way:

$$F(\varphi) = \left(\frac{1}{\sum_{k=1}^{N} \sin\theta_k} \sum_{k=1}^{N} \sin\theta_k H(\varphi - \varphi_k) \right) \times 100(\%), \tag{4}$$

where $H(\varphi)$ is the Heaviside unit step function. $F(\varphi)$ with $\sin\theta_k$ as weight shows the cumulative percentage of the number of branches.

The cumulative azimuthal distribution defined above is calculated for all five samples. From the results (not shown), it could be seen that the cumulative distribution is almost exactly a straight line with the slope of 100/180. For various compacted packings, each sample does not seem to have any distinct characteristics. Thus, we conclude that the structure of the obtained random packings before and after compaction is isotropic in the horizontal, x–y, plane in terms of the branch orientations; note that the compaction direction agrees with the gravity direction.

Next, we examine the cumulative zenithal distribution of branch orientations. Similarly to the cumulative azimuthal distribution, θ_k should be replaced by $\pi - \theta_k$ if it is in $(\pi/2, \pi]$. We rearrange the branches in ascending order of azimuthal angles in the range of $(0, \pi/2]$. Since the circle made by $\theta = \theta_k$ on a sphere of unit radius is $2\pi \sin\theta_k$ in circumference, the cumulative frequency of branches per unit area of the sphere $F(\theta)$ is defined by

$$F(\theta) = \left(\frac{1}{\sum_{k=1}^{N} \frac{1}{\sin\theta_k}} \sum_{k=1}^{N} \frac{H(\theta - \theta_k)}{\sin\theta_k} \right) \times 100(\%). \tag{5}$$

The cumulative frequency is calculated for all samples. From the results, we have found that the cumulative frequency distribution is not linear at all and that it could be represented well by a linear term and a truncated Fourier series:

$$F(\theta) = a_0\theta + \sum_{m=1}^{3} \frac{a_m}{2m} \sin 2m\theta, \tag{6}$$

where the four coefficients a_m have been determined by the least square method and are shown in Table 2.

Differentiating Eq. (6) with respect to θ, we obtain following:

$$\frac{\mathrm{d}F(\theta)}{\mathrm{d}\theta} = \sum_{m=0}^{3} a_m \cos 2m\theta \tag{7}$$

This equation shows the zenithal distribution of branches itself and its curve is drawn in Fig. 5 for the compaction coefficients $\beta = 0.0$, 0.1 and 0.2. It is seen that the maximum frequency arises between 50° and 60° while the minimum appears at $\theta = 90°$. At $\theta = 0°$, the frequencies increase with increasing compaction coefficient because new contact points of the normal direction are created. From setting the derivative of Eq. (7) to zero, $\mathrm{d}^2F(\theta)/\mathrm{d}\theta^2 = 0$, we can obtain the peak angle of the zenithal distribution. The peak angle of the distribution is $\theta = 50.1°$ for non-compacted condition, while the peak is $\theta = 57.3°$ for $\beta = 0.2$. From this result, it is found that the peak position moves toward the larger angle because the branches incline due to the axial compaction.

Table 2
Four coefficients a_m determined by the least square method

β	a_0	a_1	a_2	a_3
0.00	1.10031	−7.30224	−38.1846	7.72467
0.02	1.10022	−7.95877	−36.9211	10.0732
0.04	1.10090	−8.2719	−35.0139	11.5829
0.06	1.10196	−8.56026	−33.0232	12.9321
0.08	1.10288	−8.61198	−30.828	14.3118
0.1	1.10421	−9.05858	−28.8495	15.5073
0.12	1.10566	−9.21828	−26.5655	16.6609
0.14	1.10739	−9.39827	−24.2339	17.6660
0.16	1.10932	−9.39076	−21.6912	18.5922
0.18	1.11127	−9.12457	−18.9207	19.4361
0.20	1.11355	−9.17975	−16.4118	19.9658

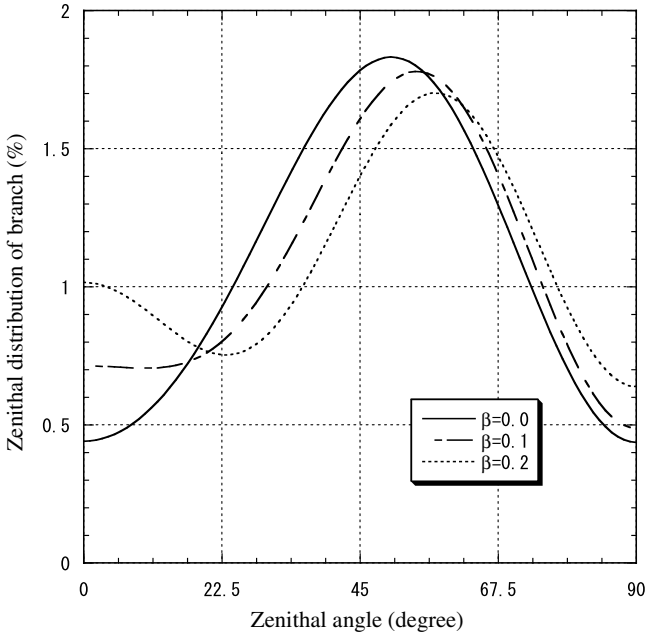

Fig. 5. Zenithal distributions of branch orientations obtained from fitting curve given by Eq. (6) for compaction coefficient $\beta = 0.0$, 0.1 and 0.2.

From the arguments so far in this sub-section, we can conclude that the packing structures are of transverse isotropy, indicating the effect of the compaction added to that of gravity.

4. Conductivity of uniaxially compacted/sintered particle aggregates

We evaluate macroscopic thermal conductivities of a uniaxially compacted and sintered particle aggregate with such statistical properties as described in the above. We regard the sintered aggregate as a random network of resistors, whose thermal resistance is evaluated by the finite element method (FEM), and then evaluate the "node" temperatures at all ends of the resistors by use of the Kirchhoff current law. Finally, we calculate the macroscopic thermal conductivities of the aggregate from the total heat flux and node temperatures.

4.1. Geometry of compaction of sintered particle pair

First, we calculate by the FEM the inverse thermal resistance ratio K/K_0 of a compacted sintered pair of spheres, which is shown in Fig. 6, picked out from the aggregate; K_0 is the inverse of the axial thermal resistance of a cylindrical solid bar with the same diameter and length as those of the spherical particles, while K the counterpart of the compacted sintered pair of spheres.

In sintering of the particle aggregate, necks are created around contact points between spheres by mass diffusion; the necks grow up with sintering time. To describe the sintered geometry, we add, around the overlaps caused by the artificial reduction in sphere-center distances, some appropriate amount of mass of the same substance as that of the particles; the added volume is the shaded portion bounded by the two overlapped particles and a torus touching both of them, as shown in Fig. 6. The geometry made by adding the mass is not exactly the same as that of real sintered particles but, at least, the shape of void space in the mass-added aggregate is much more similar to the real one than the infinitely long needle shape of vacancy, which was assumed when the self-consistent models were applied [2,3], or spheroids generally assumed in the composite models.

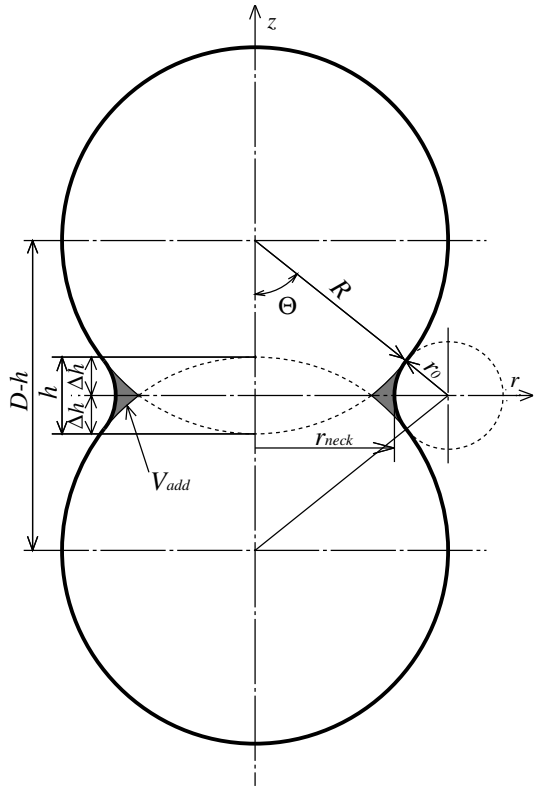

Fig. 6. Geometry of two compacted spheres with added volume (neck).

The added-mass volume per a pair of particles can be obtained by a simple geometrical consideration: see Appendix A. In what follows, we will adopt the angle Θ or the normalized radius r_0/R as a parameter of the sintering degree.

4.2. FEM analysis of thermal resistance of a sintered pair of particles

We consider the resistance of the compacted/sintered pair of particles, whose geometry is shown together with the cylindrical coordinate system (r, z) in Fig. 6.

In the analysis, neither heat conduction nor convection in the vacant space of the sintered particles and no radiation into the space are assumed, but only the heat conduction through the solid matrix of the aggregate is taken into account; so that the surfaces of the pair are insulated, that is, $\partial T/\partial n = 0$ on these surfaces; T and n are the temperature and the outward unit normal to them, respectively. For the sake of simplicity, the boundary conditions at both

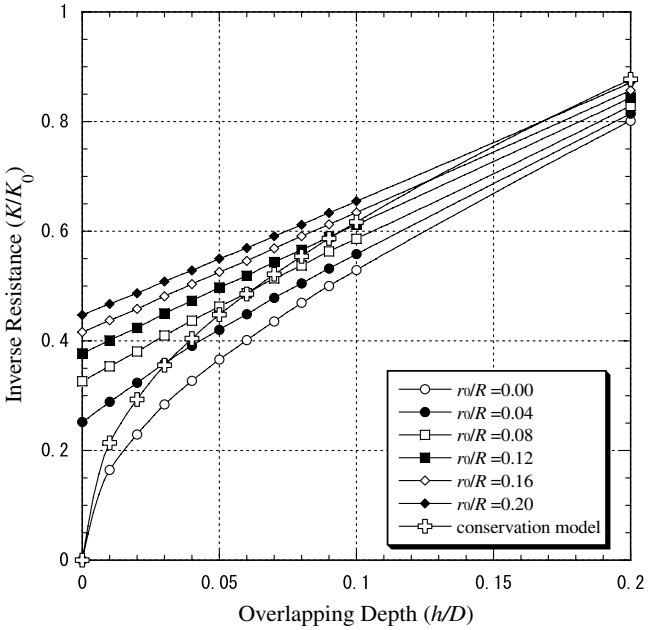

Fig. 7. Inverse resistance versus overlapping depth for two-parameter model with various meniscus radii and for conservation model.

ends of the pair are assumed to be given by $T = \pm\Delta T_0/2$, respectively. For the finite element analysis, an arbitrary cross section through the z axis is divided into finite triangles, leading to triangular ring elements because of the axisymmetric geometry.

The inverse resistance ratios K/K_0 of the sintered particle pair versus the overlapping depth h are given in Fig. 7, by the hollow cross markers for the conservation model and by various markers for the two-parameter model (various sintering degree radius ratios r_0/R ranging from 0.0 to 0.2 with their increment being 0.04).

To begin with, let us see the curves by the two-parameter model. For $r_0/R = 0.0$, the inverse resistance is zero for $h/D = 0.0$ because of the point contact. The inverse resistance rapidly increases with the overlapping depth h/D up to $h/D = 0.05$ and almost linearly increases after this point. For $r_0/R \geqslant 0.04$, these inverse resistance ratios almost linearly increase with increasing overlapping depth. The larger r_0/R, the larger the inverse resistance.

Next, let us move to the curve by the conservation model. It starts from the origin and rises up more rapidly than that for $r_0/R = 0.0$ by the two-parameter model. Its more rapid rise makes it catch up and overtake all the other curves for $r_0/R \geqslant 0.04$ by the two-parameter model, with its slope declining.

These inverse resistance ratios will be used to evaluate the macroscopic conductivity of the aggregate in the following sub-sections.

4.3. Random network of thermal resistors

In order to evaluate the macroscopic conductivity of the uniaxially compacted and sintered particle aggregate, we will replace the aggregate by a "random network" of resistors with the resistance estimated in the above. In evaluating the conductivity, we need continual resistance of resistors, which is determined as follows. First, we express the results of the finite element analysis as a function of the compaction degree as

$$\frac{K}{K_0} = C_0\left(\frac{h}{D}\right)^{C_1} + C_2\left(\frac{h}{D}\right)^{C_3} + C_4, \tag{8}$$

where C_0, C_2, C_4 are the constants to be determined by the least square method after the exponents C_1 and C_3 of (h/D) are fixed by the trial and error method. All these constants are listed in Table 3. We calculate all branch lengths in the random network, from which the compaction degree is calculated. From the regression curve in Eq. (8), we can obtain required resistance of any resistor in analyzing the network.

Table 3
Fitting parameters for curves of resistance of resistors

Model	C_0	C_1	C_2	C_3	C_4
Conservation model	2.217	2.402	1.714	0.45	0
$r_0/R = 0.00$	3.221	2.345	1.627	0.5	0
$r_0/R = 0.04$	2.372	0.817	−0.166	0.5	0.252
$r_0/R = 0.08$	2.307	0.908	−0.074	0.5	0.326
$r_0/R = 0.12$	2.269	0.981	−0.004	0.5	0.377
$r_0/R = 0.16$	2.238	1.017	0.013	0.5	0.416
$r_0/R = 0.20$	2.234	1.047	0.022	0.5	0.447

We assign specific temperatures to the nodes (or resistors' ends, which are situated at the particles' centers) existing within the outermost layers of thickness $D/2$ in a cubic box webbed by the resistors; the values of these assigned temperatures are determined so as to be proportional to the corresponding values of coordinate in the macroscopic heat flow direction, with the temperatures being zero and a given T_0 at the two opposite surfaces of the cube. The other four surfaces are assumed to be insulated. Thus, the Kirchhoff current law determines temperatures at all nodes.

Consider a central cross section of the box orthogonal to the direction of macroscopic heat flow and denote the total number of resistors crossed by this cross section as N. The total heat flow rate Q_{total} can be estimated by

$$Q_{\text{total}} = \sum_{i=1}^{N} \frac{\Delta T_i}{R_i}, \tag{9}$$

where R_i is the resistance of the ith resistor evaluated by the FEM. The macroscopic conductivity is given by dividing the total flow rate by the temperature difference T_0 between those at the box top and bottom.

5. Discussion

5.1. Validity of network model

Before proceeding to discussion of the simulation result, we will check validity of the present network model. We have applied this model (using the same computer program) to the simple cubic packing and obtained the curve of its macroscopic conductivity. Fig. 8 shows the curve of

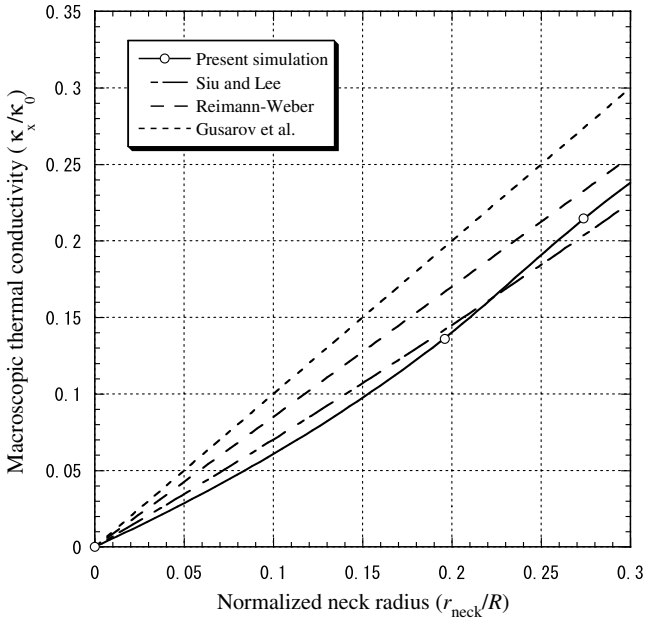

Fig. 8. Macroscopic conductivity for simple cubic packing versus normalized radius. Comparison between present model and other models.

macroscopic conductivity against the non-dimensional neck size denoted by r_{neck}/R, together with the three curves borrowed from the figure drawn by Gusarov et al. [21]; they concluded that the three curves satisfactorily agree with each other at least in the case of smaller neck size. It can be seen from the figure that the present result is also in similar agreement with the existing three results; especially with that by Siu and Lee [22], although the present curve shows slightly stronger nonlinearity than theirs. It may be concluded from this agreement that the network model is validated.

5.2. Macroscopic thermal conductivity

The macroscopic conductivities in the X and Z directions of the sintered powder aggregates for several different compaction degrees for Sample 1 are shown in Fig. 9a and b, respectively, for the two-parameter model. In these figures, the ordinate presents their macroscopic thermal conductivity κ normalized by that of the particle substance κ_0, while the abscissa is for the porosity of the sintered aggregates. Although we present only graphs for Sample 1, we have calculated both the conductivities for all samples. Since little difference among all the samples could be seen, we can say that the sample size of $B/D = 16$ is large enough to estimate the conductivity in a required accuracy.

Let us see how the conductivity depends on the degree of sintering and compaction. For a given compaction degree, the smaller degree of sintering causes the conductivity to decrease due to the larger resistance at the thinner necks. Increases in the compaction degree raise the conductivity curves as a whole, especially more for the higher degree of sintering, and shift them toward lower porosity, because the aggregates become dense.

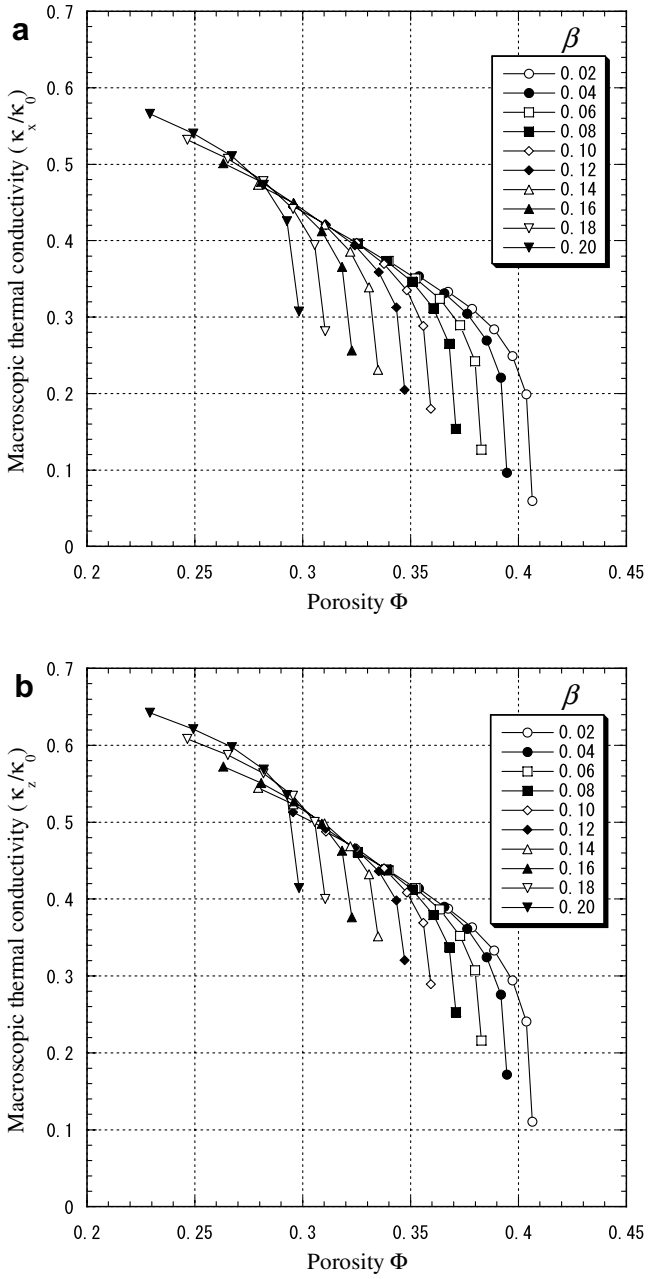

Fig. 9. Macroscopic thermal conductivity along X and Z axes (top and bottom, respectively).

Next, we examine how the thermal conductivity differs according to its direction. Comparison between (a) and (b) shows that the macroscopic thermal conductivity in the Z direction is roughly 20% larger than that in the X direction for $r_0/R = 0.02$. On the other hand, the thermal conductivity in the X direction is almost exactly equal to that in the Y direction, as we have numerically confirmed but do not illustrate it here. This reveals that the simulated packing structure is of isotropy in the X–Y plane and of anisotropy normal to this plane.

Finally, we focus on the effect of the compaction on the degree of anisotropy. We consider the case of no added mass in which $r_0/R = 0.0$ to take out only influence of

the compaction. In this case, the macroscopic thermal conductivity in the Z direction is roughly 20% larger than that in the X direction for $\beta = 0.0$ (no compaction), but roughly 30% larger for $\beta = 0.2$ (considerable compaction). Thus, roughly speaking, the increase in the conductivity due to the compaction is 10%. Although this is smaller than we expected, this may be partly understood from the fact that the compaction does not increase the coordination number so much (from 6.019 to 6.876); this small increase may come from the uniaxial (not isostatic) compaction.

It may be important for practical purposes to express all the thermal conductivities in terms of the two geometrical parameters r_0/R and β. The expressions are determined by the conventional least square method and given as follows:

$$\frac{\kappa_x}{\kappa_0} = \left(-8.81\times10^{-2} - 4.76\times10^{-2}\left(\frac{r_0}{R}\right)^{0.2} + 1.34\left(\frac{r_0}{R}\right)^{0.4}\right)\beta^{0.2} + \left(9.56\times10^{-1} - 3.0\times10^{-1}\left(\frac{r_0}{R}\right)^{0.2} - 0.81\left(\frac{r_0}{R}\right)^{0.4}\right)\beta^{0.6} \quad (10)$$

$$\frac{\kappa_z}{\kappa_0} = \left(3.95\times10^{-2} - 5.55\times10^{-1}\left(\frac{r_0}{R}\right)^{0.2} + 2.04\left(\frac{r_0}{R}\right)^{0.4}\right)\beta^{0.2} + \left(1.04 + 8.46\times10^{-1}\left(\frac{r_0}{R}\right)^{0.2} - 2.67\left(\frac{r_0}{R}\right)^{0.4}\right)\beta^{0.6} \quad (11)$$

These equations describe the simulation results for $0.0 \leqslant r_0/R \leqslant 0.2$ and $0.02 \leqslant \beta \leqslant 0.2$ to within 5% in all cases.

5.3. Comparison with result by conservation model

Here, we consider the conservation model, which has been defined in Section 2.3. We have introduced a further restriction that the overlap volume of the particle pair equals the added volume corresponding to the sintering. Equating Eqs. (A1)–(A5) in Appendix A, we can determine the sintering degree angle Θ by iteration.

Fig. 10 shows the macroscopic thermal conductivities in the X and Z directions by the conservation model (denoted by the squares and the circles, respectively) together with the results for $r_0/R = 0.0$ (no added volume) by the two-parameter model; the former model is depicted by the solid markers while the latter by the hollow marker. Further addition of a curve is made for the conductivity of the simple cubic packing estimated by the conservation model.

The thermal conductivity in the X direction is a little larger in the whole shown range of porosity if estimated by the conservation model than when estimated by the two-parameter model with $r_0/R = 0.0$. In contrast, as the compaction degree increases and subsequently the porosity decreases, the difference in the conductivity in the Z direction between the two models becomes larger. In the conservation model, the added volume decreases as the sphere pair axis inclines against the compaction direction, so that the conductivity is not so affected by the volume conservation in the X direction while it is much more affected by it in the Z direction.

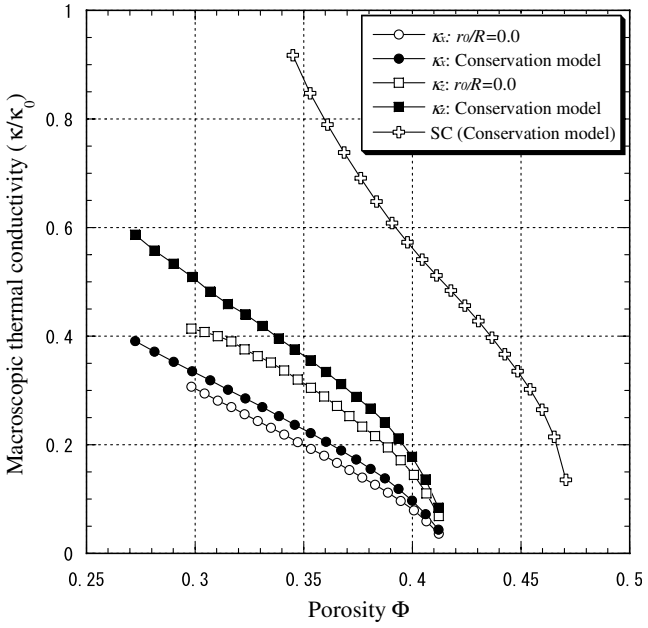

Fig. 10. Macroscopic thermal conductivities versus porosity for present random packings (two-parameter model with zero meniscus radius and conservation model, each in X and Z directions) and for simple cubic packing.

Comparison of the conductivity of the random packing, in both directions and by both models, with that of the simple cubic packing shows a remarkable difference. The difference shows that the simulation is necessary of macroscopic properties of the random packings, independently of that of the cubic packings, although both the packings have almost the same coordination number.

The macroscopic thermal conductivities for the conservation model can be described as a function of β only.

$$\frac{\kappa_x}{\kappa_0} = 4.16\times10^{-2} + 1.85\beta - 6.32\times10^{-1}\beta^2 \quad (12)$$

$$\frac{\kappa_z}{\kappa_0} = 9.44\times10^{-2} + 2.79\beta - 1.91\beta^2 \quad (13)$$

These equations describe the simulation results for $0.02 \leqslant \beta \leqslant 0.2$ to within 2% in all cases.

6. Conclusion

We have proposed a simulation method for macroscopic thermal conductivities of uniaxially compacted/sintered particle aggregates. In the first half, we have constructed random packings by a sequential free fall of particles and examined various statistical characteristics of packing structures of the compacted aggregates. In the last half, we have estimated the macroscopic thermal conductivity of the aggregates by analyzing the thermal resistor networks.

For the statistical characteristics, the following conclusions have been obtained: Branches lie more frequently

around the direction of $\theta = 50.1^\circ$ for non-compacted condition, while $\theta = 57.3^\circ$ for some compaction ($\beta = 0.2$). It is found that the peak position moves toward the larger angle because the branches incline due to compaction.

For the macroscopic thermal conductivity of the uniaxially compacted particle aggregates, the following have been concluded: the conductivities are greatly different from those of simple cubic packings, although both the packings have almost the same coordination number, and anisotropy in the conductivity is induced by the compaction in addition to gravity. The conductivities are expressed as a function of the compaction and sintering degrees for practical purposes.

Appendix A. Calculation of neck and overlap volumes

In this Appendix, we calculate the neck and overlap volumes between two particles. The geometry is indicated in Fig. 5. Knowing the overlap depth h and the radius R of identical spheres, the volume of overlap can be easily obtained as follows:

$$\frac{V_{\mathrm{lap}}}{2\pi R^3} = \frac{1}{3}\left(\frac{\Delta h}{R}\right)^2\left(3 - \frac{\Delta h}{R}\right) \tag{A1}$$

The remaining variables defined in Fig. 5 are found from the following geometric relations:

$$R(1 - \cos\Theta) = \Delta h + r_0 \cos\Theta \tag{A2}$$

The added volume is given by

$$V_{\mathrm{add}} = 2\pi \int_0^{r_0\cos\Theta} [\{(r - \Delta h)^2 \tan^2\Theta + r_0^2 - \Delta h(2R - \Delta h)\} - 2(R - \Delta h)z - 2(R - \Delta h)\tan\Theta\sqrt{r_0^2 - z^2}]\mathrm{d}z \tag{A3}$$

Here, the terms in the first and second braces in the integrand present square of the outer and inner radii of the annulus shown by the shade. The integral from $z = 0$ to $z = r_0\cos\Theta$ can be estimated by use of the following formula:

$$\int_0^{r_0\cos\Theta} \sqrt{r_0^2 - z^2}\mathrm{d}z = \frac{1}{2}r_0^2\cos\Theta\sin\Theta + \frac{1}{2}r_0^2\left(\frac{\pi}{2} - \Theta\right) \tag{A4}$$

Thus, the added volume reduces to:

$$\begin{aligned}\frac{V_{\mathrm{add}}}{2\pi R^3} = &-\left(1 - \frac{\Delta h}{R}\right)\left(\frac{1 - \cos\Theta - \Delta h/R}{\cos\Theta}\right)^2 \\ &\times \left(1 + \sin^2\Theta + \tan\Theta\left(\frac{\pi}{2} - \Theta\right)\right) \\ &+ \left(1 - \frac{\Delta h}{R}\right)\left(\frac{1 - \cos\Theta - \Delta h/R}{\cos\Theta}\right)^2 \tan\Theta\left(1 - \cos\Theta - \frac{\Delta h}{R}\right) \\ &- \frac{\Delta h}{R}\left(2 - \frac{\Delta h}{R}\right)\left(1 - \cos\Theta - \frac{\Delta h}{R}\right)\end{aligned} \tag{A5}$$

References

[1] L.J. Gibson, M.F. Ashby, Cellular Solids: Structure and Properties, second ed., Cambridge University Press, Cambridge, 1997.

[2] R. Hill, Self-consistent mechanics of composite materials, J. Mech. Phys. Solids 13 (1965) 213–222.

[3] M. Taya, R.J. Arsenault, Metal Matrix Composite, Pergamon Press, New York, 1989.

[4] M. Kurashige, T. Hayashi, K. Imai, Simulated effective elastic moduli and wave velocities in water-saturated sintered glass-beads, Acta Mech. 132 (1999) 177–194.

[5] M. Kurashige, M. Mishima, K. Imai, Simulated effective thermal conductivity of sintered, randomly packed spheres and statistical structures of packings, J. Therm. Stress. 22 (1999) 713–733.

[6] H. Kato, C. Matsunaga, M. Kurashige, K. Imai, Anisotropy in packing structure and elasticity of sintering spherical particles, JSME Int. J. Ser. A 45 (4) (2002) 585–595.

[7] Ik-H. Oh, N. Nomura, S. Hanada, Microstructures and mechanical properties of porous titanium compacts prepared by powder sintering, Mater. Trans. 43 (3) (2002) 443–446.

[8] N. Nomura, M. Abe, A. Kawamura, S. Fujinuma, A. Chiba, N. Masahashi, S. Hanada, Fabrication and mechanical properties of porous Co–Cr–Mo alloy compacts without Ni addition, Mater. Trans. 47 (2) (2006) 283–286.

[9] C.L. Martin, D. Bouvard, Isostatic compaction of bimodal powder mixtures and composites, Int. J. Mech. Sci. 46 (2004) 907–927.

[10] C.L. Martin, D. Bouvard, Study of the cold compaction of composite powders by the discrete element method, Acta Mater. 51 (2003) 373–386.

[11] C.L. Martin, D. Bouvard, S. Shima, Study of particle rearrangement during powder compaction by the discrete element method, J. Mech. Phys. Solids 51 (2003) 667–693.

[12] K.T. Kim, S.C. Lee, H.S. Ryu, Densification behavior of aluminum alloy powder mixed with zirconia powder inclusion under cold compaction, Mater. Sci. Eng. A 340 (2003) 41–48.

[13] P. Redanz, N.A. Fleck, The compaction of a random distribution of metal cylinders by the discrete element method, Acta Mater. 49 (2001) 4325–4335.

[14] I. Taguchi, M. Kurashige, K. Imai, Effects of cubic container's wall or floor on random packing structures of spherical particles, JSME Int. J. Ser. A 49 (2006) 265–272.

[15] B.A. Wichmann, I.D. Hill, An efficient and portable pseudo-random number generator, Algorithm AS, Roy. Statist. Soc. 183 (1982) 188–190.

[16] D.P. Haughey, G.S.G. Beveridge, Structural properties of packed beds, Can. J. Chem. Eng. 47 (1969) 130–140.

[17] E.M. Tory, B.H. Church, M.K. Tam, M. Ratner, simulated random packing of equal sphere, Can. J. Chem. Eng. 51 (1973) 484–493.

[18] M. Kurashige, K. Imaida, Y. Goto, Phase velocity measurement for three bulk waves in water-saturated sintered glass beads by an ultrasonic mode conversion method, in: Proceedings of International Symposium on Impact Engineering, Sendai, vol. 2, 1992, pp. 508–513.

[19] S. Torquato, Random Heterogeneous Materials: Microstructure and Macroscopic Properties, Springer-Verlag, New York, 2001.

[20] I. Taguchi, M. Kurashige, Macroscopic elastic properties of randomly packed balloons, J. Mech. Mater. Struct. 2 (2007) 529–555.

[21] A.V. Gusarov, T. Laoui, L. Froyen, V.I. Titov, Contact thermal conductivity of a powder bed in selective laser sintering, Int. J. Heat Mass Transfer 46 (2003) 1103–1109.

[22] W.W.M. Siu, S.H.-K. Lee, Effective conductivity computation of a packed bed using constriction resistance and contact angle effects, Int. J. Heat Mass Transfer 43 (2000) 3917–3924.